Journal of
Micro/Nanolithography,
MEMS, and MOEMS

Nanolithography.SPIEDigitalLibrary.org

Impact of B_4C capping layer for extreme ultraviolet mask on the sensitivity of patterned mask inspection using a projection electron microscope

Susumu Iida
Ryoichi Hirano
Tsuyoshi Amano
Hidehiro Watanabe

SPIE.

Impact of B_4C capping layer for extreme ultraviolet mask on the sensitivity of patterned mask inspection using a projection electron microscope

Susumu Iida,* Ryoichi Hirano, Tsuyoshi Amano, and Hidehiro Watanabe
EUVL Infrastructure Development Center, Inc., 16-1 Onogawa, Tsukuba-shi, Ibaraki-ken 305-8569, Japan

Abstract. The inspection sensitivity of a patterned extreme ultraviolet mask with B_4C-capped multilayer (ML) was investigated using a simulated projection electron microscope (PEM) image. Extrusion and intrusion defects with 16-nm size were detected with their intensity of >10 times the standard deviation of the background level on a half-pitch 64-nm line-and-space pattern. The defect detection sensitivity in this case was higher than that of a Ru-capped ML sample and has a potential to meet the requirement for beyond 16-nm node generation from the standpoint of patterned mask inspection using the PEM technique. These results indicate that the B_4C capping layer, besides its good durability, has an advantage for high sensitivity of patterned mask inspection. The optimal condition of the incident beam energy was found to be 500 and 1,000 eV for the samples of B_4C-capped ML and B_4C-buffered Ru-capped ML, respectively. The sensitivity of defect detection was strongly affected by the difference of secondary electron emission coefficients (SEECs) between the absorber layer and capping layer. However, the small incident beam energy was found to be preferable when the SEEC difference was relatively high. [DOI: 10.1117/1.JMM.13.4.043015]

Keywords: extreme ultraviolet mask; B_4C; defect detection; pattern inspection; Monte Carlo simulation; projection electron microscope.

Paper 14151P received Oct. 10, 2014; accepted for publication Nov. 17, 2014; published online Dec. 11, 2014.

1 Introduction

Extreme ultraviolet lithography (EUVL) is a promising technique for post-2X nm generation lithography. Pattern inspection is one of the key issues to be addressed in the fabrication of devices of half pitch (hp) 16 nm and beyond. Continued shrinkage of pattern size has been leading to difficulties in detecting small defects.[1] Improvement in image resolution is realized by using an electron beam as used in the SEM-type inspection systems, but because of the very small electron-beam spot size used in such systems, it takes too much time for inspection. Therefore, we have been developing a projection electron microscope (PEM)[2,3] for pattern inspection and have evaluated its feasibility.[4–7] In order to accelerate this development program, the optimal inspection condition was investigated by using a computer simulation.[8–11] We already reported that 16-nm-sized defect on hp 64-nm mask pattern was detectable with a 10-times higher signal intensity than that of the standard deviation of the background intensity level by using the PEM technique when the Ru capped multilayer (ML) was used in EUV mask,[9] and the simulated detectability was found to be in good agreement with experimental results.[7] It was also found that the sensitivity of defect detection was predictable by measuring the secondary electron yield curves of a Ta-based absorber layer and Ru-capped ML. This result suggests that the EUV mask structure affects the optimal inspection condition.[9,10] As a capping layer, nondoped Si, 11-nm thick, had been investigated. However, because of its disadvantages, such as prone to oxidation, low chemical resistance, and low etch selectivity, 2.5-nm-thick Ru has been used to replace Si.[12] Recently, Jang et al. reported that B_4C has a better durability for cleaning and has better chemical, mechanical, and electrical resistance and optical properties than Ru.[13] In this paper, the proposed mask structures, such as B_4C-capped ML and B_4C-buffered Ru-capped ML, were investigated from the standpoint of pattern mask inspection and analyzed for their optimal conditions using a PEM technique.

2 Experimental

In order to simulate defect inspection by a PEM technique, simulated images were obtained using CHARIOT Monte Carlo software (Abeam Technologies, Inc.).[14] The software with 72 cores was installed in an all-in-one server computer, Proliant DL 980 G2 (Hewlett-Packard) with 80 cores. Figure 1 shows the schematic representations of a sample EUV mask used for the simulation. On this mask, defects with various sizes were fabricated on hp 64-nm line-and-space (L/S) patterns. Ta-based absorber layers with 66-nm thickness were fabricated on EUV reflective MLs. In order to investigate the impact of capping layer for the MLs on the sensitivity of defect detection, three types of capping layers were used: (1) 2.5-nm-thick Ru, (2) 2.5-nm-thick B_4C, and (3) 1.25-nm-thick Ru on 1.25-nm-thick B_4C. The third one is called as B_4C-buffered Ru capped ML.[13] The MLs contained 40 pairs of 3-nm-thick Mo and 4-nm-thick Si. The thicknesses of the defects were 66 nm, which was the same as that of the absorber layers. Sizes of the defects were 64 nm × 64 nm, 32 nm × 32 nm, 22 nm × 22 nm, and 16 nm × 16 nm. According to the ITRS-2013 update, the defect size on the EUV mask is defined as the square root

*Address all correspondence to: Susumu Iida, E-mail: susumu.iida@eidec.co.jp

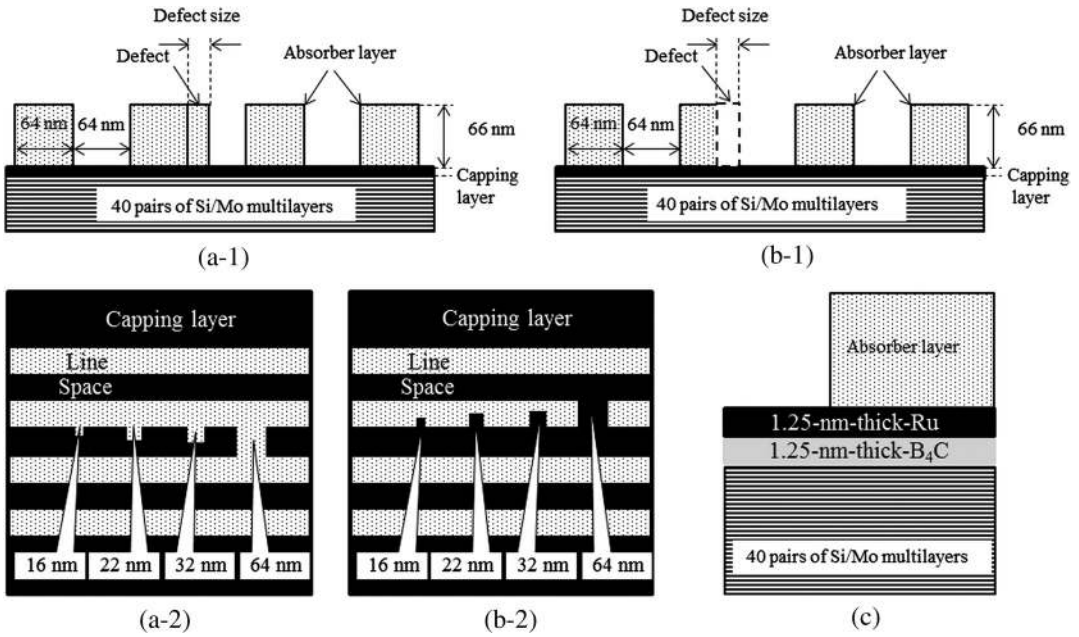

Fig. 1 Schematic representations of a sample extreme ultraviolet mask used for the simulation. The cross-sectional and top views of the sample [(a-1) and (a-2)] with extrusion defects and [(b-1) and (b-2)] with intrusion defects, and (c) the cross-sectional view of B_4C-buffered Ru capped multilayer (ML) sample.

of the defect area on a two-dimensional mask surface. Because all the defects in this study were square ones, hereafter, we refer to them as 64-, 32-, 22-, and 16-nm defects. In order to improve the reliability of the simulation result, a secondary electron yield curve of the utilized materials was applied for the calibration of the simulation result. The secondary electron emission coefficient (SEEC) of the samples was measured using a specially designed scanning Auger microscope (SAM). The detailed method for measuring the SEEC using SAM is described elsewhere.[15] Densities of B_4C and Ru with 2.52 and 12.45 g/cm^3 were input to a database of the simulator, respectively. The current density and the dwell time were 1.9×10^{-1} A/cm^2 and 1 ms, respectively. The pixel size of the image detector was 16 nm × 16 nm, and the average number of electrons per pixel corresponded to 3,000 electrons per pixel. Incident electrons with energies of 50, 250, 500, 1,000, and 3,000 eV were used to investigate the influence of the incident beam energy on the defect inspection. The difference between the simulated PEM image with defects and that without defects is defined as difference image. In order to define the sensitivity of defect detection, we identified the signal intensity in the difference image with more than 10 times the intensity of the standard deviation of the background intensity levels as a defect. Image processing operations were applied to the simulated image to enhance the detect signal intensities.[6,9] The detailed simulation conditions were described earlier.[9]

3 Results and Discussion

3.1 *Investigation of B_4C Capped ML*

Figure 2(a) shows the experimentally obtained SEECs of Ta-based absorber, Ru-capped ML, and B_4C-capped ML. The yield curves of Ru and B_4C-capped ML showed the

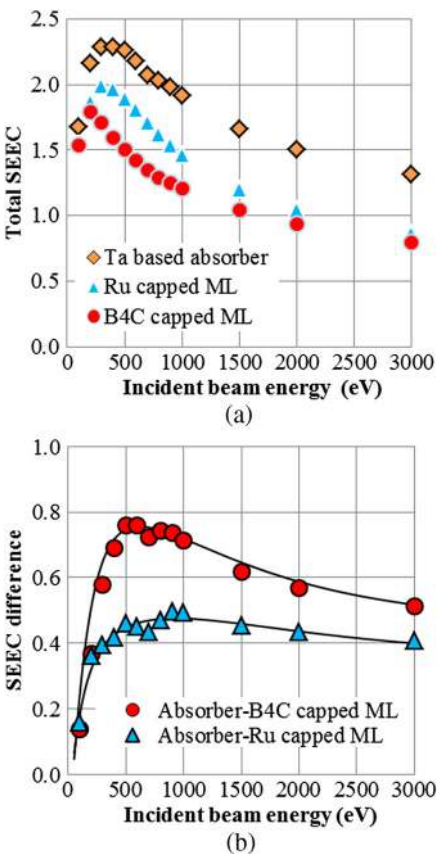

Fig. 2 (a) Experimentally obtained secondary electron emission coefficients (SEECs) of Ta-based absorber, Ru-capped ML, and B_4C-capped ML. (b) Experimental SEEC difference (which was calculated by subtracting SEEC of MLs from that of the absorber layer) as functions of incident beam energy.

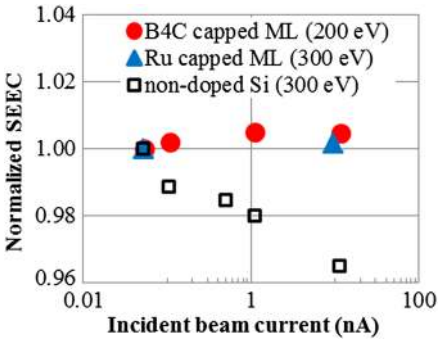

Fig. 3 Experimentally obtained SEECs of Ru-capped ML, B_4C-capped ML, and nondoped Si layer as functions of primary electron current with the energy of 200, 300, and 300 eV (the maximum values of their yield curves), respectively. The SEECs are normalized by the SEEC value for 50 pA. Diameter of the incident beam was estimated to be ~1.2 μm at 2 nA with 300 eV.

peaks at 300 and 200 eV, respectively. The overall SEECs of the B_4C sample are lower than that of the Ru one. Figure 2(b) shows the experimental SEEC difference (which is calculated by subtracting the SEEC of these MLs from that of the absorber layer) as a function of incident beam energy. In the case of Ru-capped ML, the SEEC difference has a peak near 1,000 eV. We had already reported that the incident beam energy with 1,000 eV was the most sensitive condition for extrusion defect detection, because the contrast is the highest at this condition. On the other hand, in the case of the B_4C-capped ML, the SEEC difference has a peak near 500 eV. Furthermore, the difference is 1.5 times greater than that with the case of the Ru sample. In order to examine the influence of the charging effect on the MLs, effect of incident electron current on the SEEC was investigated using three types of layers as shown in Fig. 3. The SEECs of B_4C-capped ML remain almost constant as the incident electron beam current increases, and this effect is similar to the Ru-capped ML. The SEEC of the nondoped Si layer, which had been used as the capping layer, shows a significant decrease with the increasing beam current, because the emitted SEs return back to the sample surface due to the strong positive charges involved.[16,17] These results indicate that the charging effect attributed to the B_4C-capped ML is negligibly small as is the case with Ru-capped ML; the SE signal from the B_4C-capped ML is not changed regardless of the electron dosage. Figure 4 shows the difference image between simulated PEM image with extrusion defects and that without defects. In the case of 500 eV, the 16-nm-sized defect was detected with a signal intensity more than 10 times higher than that of the standard deviation of the background intensity level (10σ). Figure 5 shows the peak intensity of the extrusion defect signal as a function of incident beam energy. This signal intensity of 16-nm defect with 500 eV is 1.3 times higher than that of the Ru sample with 1,000 eV, which is the most sensitive condition on Ru sample. The defect signal reached a maximum value at the incident beam energy of 500 eV in each size of the defect. This tendency is in good agreement with the experimentally obtained SEEC difference between the absorber layer and ML as shown in Fig. 2(b). Figure 6 shows the difference image in the case of intrusion defects. The 16-nm-sized defect was detected with $>10\sigma$ in the cases of 50, 250, 500, and 1,000 eV. These results indicate that both extrusion and intrusion defects 16 nm in size can be detected without any false defect at the incident beam energy of 500 eV. Although a false defect was observed at 1,000 eV, this can be removed by elevating the threshold (18σ), while 16-nm-sized defect remains detected as shown in Fig. 6(f). Figure 7 shows the intrusion defect signal intensity as a function of incident beam energy. The signal intensities of the intrusion defect with 16 nm size are much higher than in the case of the extrusion defect. The incident beam energy with a maximum value of the defect signal was shifted to a lower energy as the defect size decreased. The defect signal

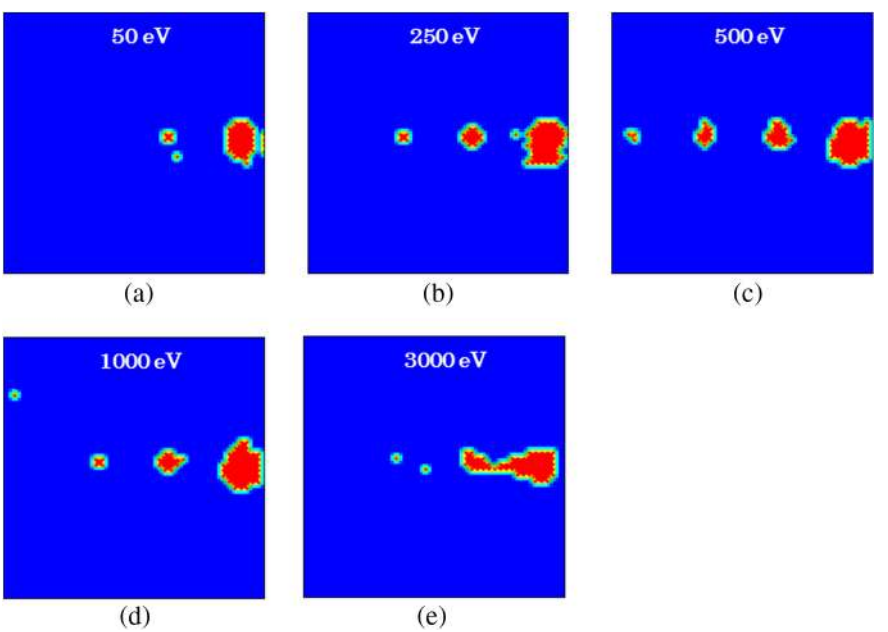

Fig. 4 The difference image for extrusion defects on B_4C-capped ML sample. The intensity values less than the threshold value (10σ) are set to zero. The incident beam energy was (a) 50 eV, (b) 250 eV, (c) 500 eV, (d) 1,000 eV, and (e) 3,000 eV.

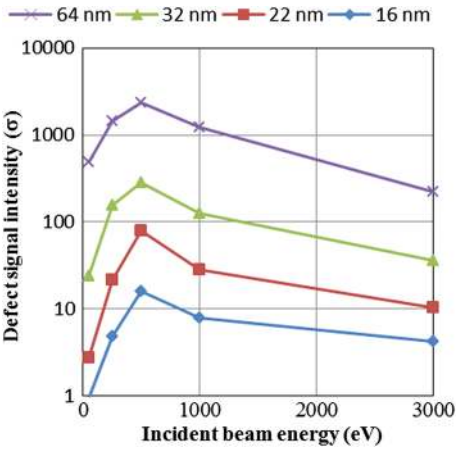

Fig. 5 The signal intensity of the extrusion defect signal as a function of incident beam energy.

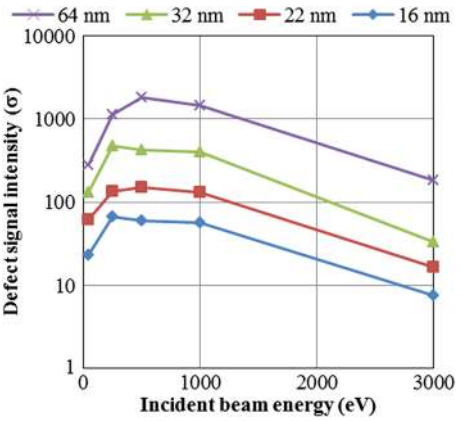

Fig. 7 The signal intensity of the intrusion defect signal as a function of incident beam energy.

reached a maximum value at 500 eV in 64-nm-sized defect, whereas in the 16-nm-sized defect, it reached a maximum value at 250 eV. The authors had already reported that a similar phenomenon was observed in the case of Ru-capped ML.[9] In the case of the intrusion defect, because the aspect ratio of the smaller defect becomes higher, the elevation angle of the defect becomes narrower as defect size gets smaller. Therefore, the signal from the bottom of the intrusion defect becomes weaker as shown in Fig. 8. This is the same mechanism as that in the case where the SE signals from the bottom of trench pattern decrease as their aspect ratios become high.[18] On the other hand, the signal around the defect generated from the absorber layer does not change even if the defect size becomes smaller. As a result, the defect signal curve corresponds to the yield curve of the absorber layer as shown in Fig. 2(a) when the defect size is comparatively small. And when the defect size is comparatively large, this behavior then corresponds to

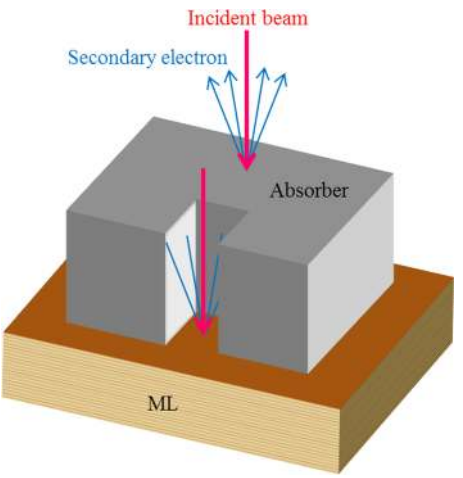

Fig. 8 Schematic illustration of the intrusion defect and the secondary electron signals blocked by the side wall of the defect.

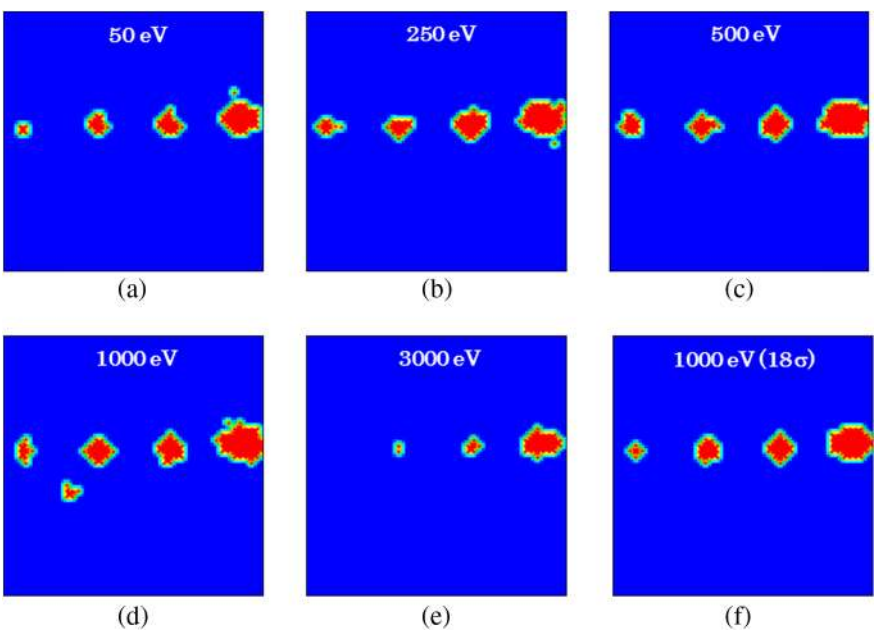

Fig. 6 The difference image for the intrusion defects on a B_4C-capped ML sample. The intensity values less than the threshold value (10σ) are set to zero. The incident beam energy was (a) 50 eV, (b) 250 eV, (c) 500 eV, (d) 1,000 eV, and (e) 3,000 eV. (f) The threshold was elevated to 18σ in order to remove the false defect observed in (d).

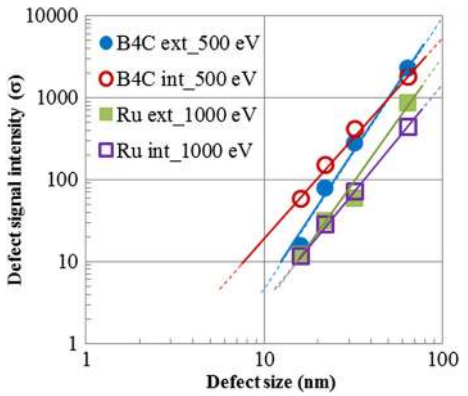

Fig. 9 The extrusion and intrusion defects signal intensities as functions of defect size in the case of Ru-capped ML with 1,000 eV and B_4C-capped ML with 500 eV.

Table 1 Extrapolated detectability limit of the defect.

	Extrusion (nm)	Extrusion (nm)
Ru-capped multilayer	15	15
B_4C-capped multilayer	13	7

the curve of SEEC difference as shown in Fig. 2(b). The detail explanation had been described elswere.[9,18] Figure 9 shows the double logarithmic plots of the defect signal intensity as functions of defect size. By fitting these plotted data with a power function, the dependence of defect signal intensity on the defect size can be analyzed as a linear regression. The detectability limits can be extrapolated from the intersection value with $\sigma = 10$. The slope of the plot for the intrusion defect is gentler than that of the extrusion defect. This result reflects the fact that the sensitivity of an intrusion defect degrades relatively less than that of an extrusion defect as the size of the defect becomes small as discussed above. Table 1 shows the extrapolated detectability limit using PEM technique. It is clearly shown that the B_4C-capped ML has an advantage due to its high sensitivity of defect detection when using the PEM inspection technique and has a potential to meet the requirements beyond hp 16-nm node from the standpoint of the patterned mask inspection. We have already established that 11-nm-sized defect on the Ru capped ML also can be detected with 10σ in the inspection condition with 10,000 electrons/pixel.[5]

3.2 *Investigation of B_4C Buffered Ru Capped ML*

Figure 10 shows the difference image in the case of extrusion defects on the B_4C-buffered Ru-capped ML. In the case of 1,000 eV, the 16-nm-sized defect was detected with $>10\sigma$. This peak signal intensity is 1.6 times higher than that of an Ru sample with 1,000 eV. Some false defects observed at 1,000 eV can be removed by elevating the threshold to 13.5σ as shown in Fig. 10(f). We already had reported that the SEEC of the Ru-capped ML was affected by the underlying Si and Mo with lower SEECs than that of Ru.[10] In the case of B_4C-buffered Ru-capped ML, the thickness of Ru is two times thinner than that of the Ru-capped ML sample. Furthermore, density and SEECs of B_4C are much lower than those of Ru. Therefore, the SEECs of B_4C-buffered Ru-capped ML are much affected by the underlying layers.[10,19] As shown in Fig. 11(a), the SEECs of B_4C-buffered Ru-capped ML were lower than those of Ru-capped ML when the incident beam energy was >600 eV, whereas those SEECs are almost the same in the range of 200 to 500 eV. These phenomena affect the sensitivity of defect inspection as shown in Fig. 11(b). The defect signal intensity is almost the same in the case of 250 and 500 eV on both samples, while, on the other

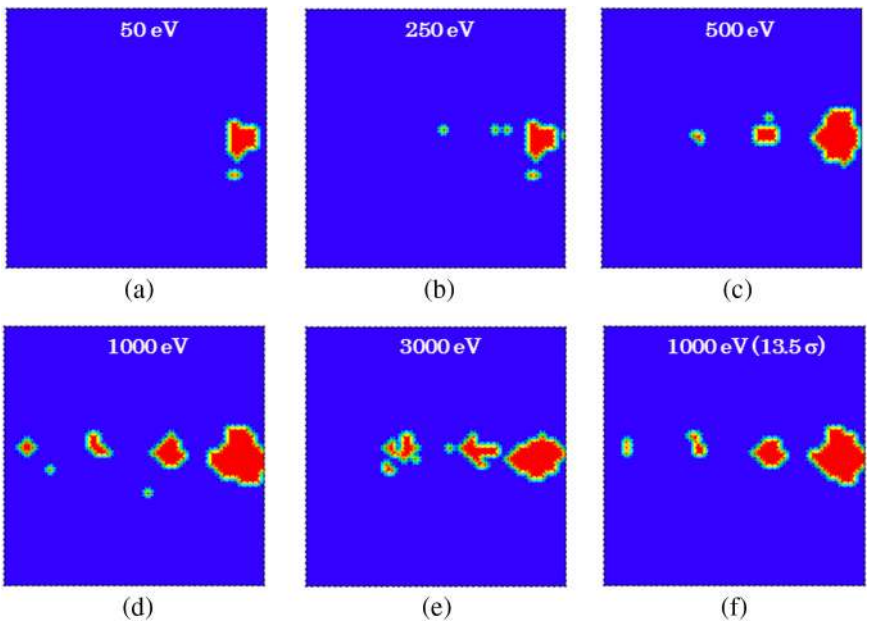

Fig. 10 The difference image for extrusion defects on B_4C-buffered Ru-capped ML sample. The intensity values less than the threshold value (10σ) are set to zero. The incident beam energy was (a) 50 eV, (b) 250 eV, (c) 500 eV, (d) 1,000 eV, and (e) 3,000 eV. (f) The threshold was elevated to 13.5σ in order to remove the false defect observed in (d).

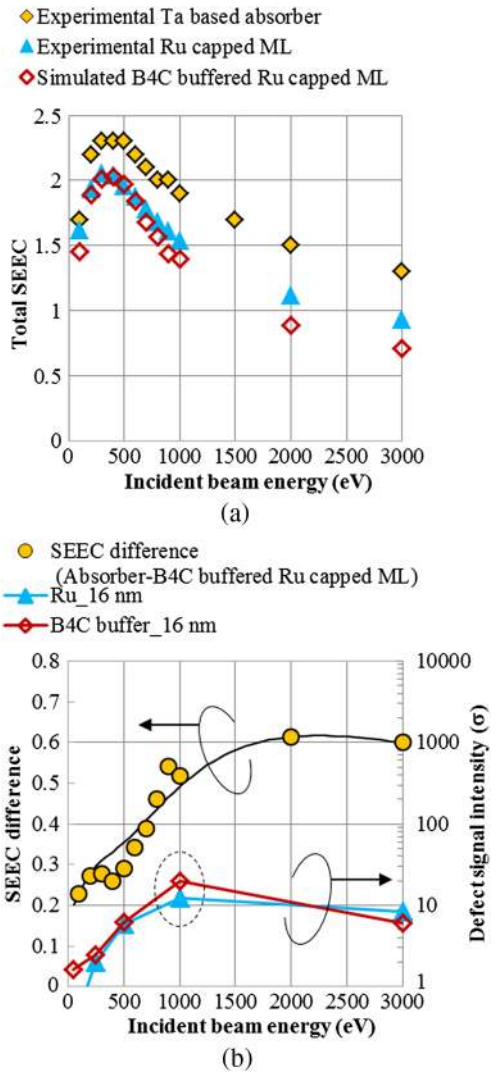

Fig. 11 (a) Experimental SEEC for Ta-based absorber and Ru-capped ML, and simulated SEEC for B_4C-buffered Ru-capped ML. (b) The defect signal intensity of the 16-nm-sized extrusion defect and the SEEC difference between Ta-based absorber layer and B_4C-buffered Ru-capped ML as functions of incident beam energy.

hand, in the case of 1,000 eV, the intensity for B_4C-buffered Ru-capped ML is 1.6 times higher than that for the Ru sample (intensities are 19.7 and 12.2, respectively) as indicated by the dashed circle in Fig. 11(b). However, in the case of 3,000 eV, the defect signal is lower than in the case of 1,000 eV in spite of the large SEEC difference. This

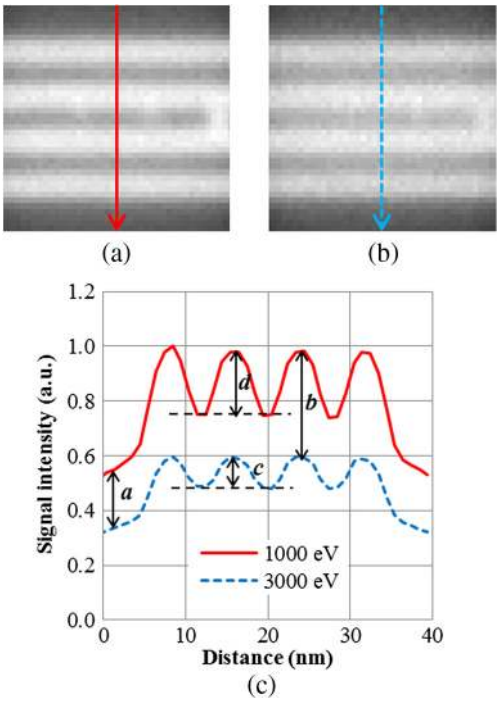

Fig. 13 Simulated images with extrusion defects on the B_4C-buffered Ru-capped ML at the incident beam energies of (a) 1,000 eV and (b) 3,000 eV. (c) Their signal intensity profiles along the arrows indicated in (a) and (b). The signal intensity is normalized by the maximum value for 1,000 eV.

phenomenon can be explained by electron scattering near the edge of a Ta-based absorber layer as shown in Fig. 12.[20] In the case of 3,000 eV, electron scattering is severe and affects the opposite side wall and bottom of the pattern as compared with 500 and 1,000 eV. Such severely scattered electrons become a source of noise and degrade the signal-to-noise ratio of the defect. Figures 13(a) and 13(b) show the simulated images with extrusion defects on the B_4C-buffered Ru-capped ML at the incident beam energy of 1,000 and 3,000 eV, respectively. The L/S patterns are observed at the center of the images, and dark areas at the top and bottom sides of the image correspond to the capping layer. It is clearly shown that a blurred image was obtained at 3,000 eV as compared with the case at 1,000 eV. Figure 13(c) shows their signal intensity profiles along the arrows indicated in Figs. 13(a) and 13(b). The intensity difference between the two conditions with 1,000 and 3,000 eV for the capping layer indicated as

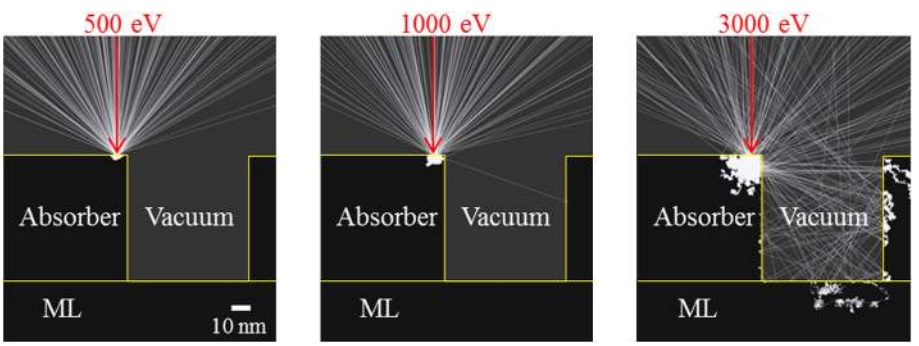

Fig. 12 Simulated electron trajectories injected near the edge of a Ta based absorber layer. The incident beam energy is 500, 1,000, and 3,000 eV.

(*a*) corresponds to its SEEC difference between these conditions. In a similar manner, the intensity difference between 1,000 and 3,000 eV for the absorber layer indicated as (*b*) corresponds to its SEEC difference between these conditions. However, peak-to-peak intensity swing of the L/S pattern signal at 3,000 eV (*c*) is smaller than that at 1,000 eV (*d*) in spite of the large SEEC difference. This is because the severely scattered electrons become the source of noise, and then the effect of the large SEEC difference is blocked by that noise. This result indicates that the sensitivity of defect detection is affected by the SEEC difference and also by electron scattering. Thus, the small incident beam energy is preferable when the SEEC difference is sufficiently high.

4 Summary and Conclusions

The inspection sensitivities of patterned EUV masks with B_4C-capped ML and B_4C-buffered Ru-capped ML were investigated using simulated PEM images. By measuring the SEECs of the mask materials, the sensitivity of defect detectability and its optimal inspection condition became predictable. The optimal condition of the incident beam energy was found to be 500 and 1,000 eV for the sample of B_4C-capped ML and B_4C-buffered Ru-capped ML, respectively. It was also found that the charging effect attributed to the B_4C-capped ML is negligible as is the case with Ru-capped ML; the SE signal from the B_4C-capped ML is not changed regardless of the electron dosage. In the case of B_4C-capped ML, both extrusion and intrusion defects with 16 nm size were detected without any false defect at the incident beam energy of 500 eV. These defect signal intensities were more than 10 times higher than the standard deviation of the background level; those intensities were much higher than those of the Ru-capped ML samples. It was found that the sensitivity of defect detection using B_4C-capped ML has a potential to meet the requirements for beyond 16-nm node generation from the standpoint of patterned mask inspection using PEM technique. These results indicate that the B_4C capping layer has an advantage for high sensitivity of patterned mask inspection besides its good durability. In the case of B_4C-buffered Ru-capped ML, the optimal condition of incident beam energy was 1,000 eV. False defects could be removed by elevating the threshold, while 16-nm-sized defect remains detected. Although the sensitivity of defect detection was strongly affected by the SEEC difference, the severely scattered electrons near the pattern edge due to high-energy incident beam become a source of noise that then blocks the effect of the large SEEC difference. This result indicates that a small incident beam energy is preferable when the SEEC difference is sufficiently high.

Acknowledgments

The authors would like to thank Ms. S. Araki of NISSAN ARC, LTD. for measuring secondary electron emission coefficients and useful discussions, and Ms. W. Asada of EUVL Infrastructure Development Center, Inc. (EIDEC) for helping in their work. This work was supported by New Energy and Industrial Technology Development Organization (NEDO).

References

1. H. Hashimoto et al., "Development of a new mask pattern inspection tool NPI-7000, and applied results to EUV mask inspection," *Proc. SPIE* **8441**, 844117 (2012).
2. M. Miyoshi et al., "Electron beam inspection system based on the projection imaging electron microscope," *J. Vac. Sci. Technol. B* **19**, 2852 (2001).
3. S. Yamaguchi et al., "Performance of EBeyeM for EUV mask inspection," *Proc. SPIE* **8166**, 81662F (2011).
4. R. Hirano et al., "Development of extreme ultraviolet mask pattern inspection technology using projection electron beam optics," *J. Micro/Nanolith. MEMS MOEMS* **12**, 021003 (2013).
5. R. Hirano et al., "Patterned mask inspection technology with projection electron microscope technique on extreme ultraviolet masks," *J. Micro/Nanolith. MEMS MOEMS* **13**, 013009 (2014).
6. H. Watanabe et al., "EUV patterned mask inspection system using a projection electron microscope technique," *Proc. SPIE* **8880**, 88800U (2013).
7. R. Hirano et al., "EUV patterned mask inspection performance of an advanced projection electron microscope (PEM) system for hp 16 nm and beyond," *Proc. SPIE* **9256**, 92560M (2014).
8. S. Iida et al., "Identification of residual-type defect on extreme ultraviolet mask by projection electron microscope using Monte Carlo simulation," *J. Vac. Sci. Technol. B* **30**(6), 06F503 (2012).
9. S. Iida et al., "Extreme ultraviolet mask defect inspection with a half pitch 16-nm node using simulated projection electron microscope images," *J. Micro/Nanolith. MEMS MOEMS* **12**, 023013 (2013).
10. S. Iida et al., "Impact of electron scattering in extreme ultraviolet reflective multilayer on electron image," *J. Vac. Sci. Technol. B* **31**(6), 06F601 (2013).
11. S. Iida et al., "Analysis of image distortion on projection electron microscope image," *Jpn. J. Appl. Phys.* **53**, 116602 (2014).
12. P. Y. Yan et al., "EUVL mask with Ru ML capping," *Proc. SPIE* **5256**, 1281–1286 (2003).
13. I. Y. Jang et al., "Ruthenium (Ru) peeling and predicting robustness of the capping layer using finite element method (FEM) modeling," *Proc. SPIE* **9256**, 92560I (2014).
14. S. Babin et al., "CHARIOT: software tool for modeling SEM signal and e-beam lithography," *Phys. Procedia* **1**, 305 (2008).
15. M. Kadowaki et al., "Investigation of factors causing difference between simulation and real SEM image," *Proc. SPIE* **7272**, 72723I (2009).
16. S. Aoyagi and K. Ura, "Initialization by erasing the surface potential of negatively charged insulators in scanning electron microscope (SEM) observation," *J. Electron Microsc.* **48**(5), 555 (1999).
17. M. Miyoshi and K. Ura, "Negative charging-up contrast formation of multilayered structures with a nonpenetrating electron beam in scanning-electron microscope," *J. Vac. Sci. Technol. B* **23**, 2763 (2005).
18. D. Bizen, Y. Sohda, and H. Kazumi, "Dependence of secondary-electron yield on aspect ratio of several trench patterns," *Proc. SPIE* **9050**, 90500K (2014).
19. N. Okai and Y. Sohda, "Simulation of electron scattering in a scanning electron microscope for subsurface metrology," *J. Vac. Sci. Technol. B* **30**(6), 06F701 (2012).
20. K. Ohya, "Simulation of secondary electron emission from a stepped surface in scanning ion microscopes," *Jpn. J. Appl. Phys.* **53**, 06JB01 (2014).

Susumu Iida received his BS and MS degrees in 1995 and 1997, respectively, and later in 2000, he earned his PhD in electronics, all from the Shizuoka University, Japan. He joined the Research and Development Center, Toshiba Corporation. In 2011, he was assigned to EIDEC, and since then, he has been engaged in the development of patterned mask inspection.

Ryoichi Hirano received his BS and MS degree in instrumentation engineering from Keio University in 1984 and 1986, respectively. He joined Toshiba Corporation, where he carried out research on semiconductor equipment technology. In 2011, he was assigned to EIDEC, and since then he has been engaged in the development of patterned mask inspection.

Tsuyoshi Amano received his BS and MS degrees in applied chemistry from Keio University in 1997 and 1999, respectively. He joined Dai Nippon Printing Co. Ltd., where he carried out research on mask process, metrology, and repair technology. In 2011, he was assigned to EIDEC, and since then he has been engaged in the development of patterned masks and blank inspection tools.

Hidehiro Watanabe received his BS and MS degrees in mineralogy from the University of Tokyo in 1983 and 1985, respectively. He joined Toshiba Corporation, where he carried out his engineering duties in the area of photo mask. In 2011, he was assigned to EIDEC, and since then he has been working as a general manager of advanced mask research department.